Neutron scattering from ^{28}Si and ^{32}S from 8.0 to 18.9 MeV, dispersive optical model analyses, and ground-state correlations

M. A. Al-Ohali,[1] J. P. Delaroche,[2,*] C. R. Howell,[3] M. M. Nagadi,[1] A. A. Naqvi,[1] W. Tornow,[3]
R. L. Walter,[3] and G. J. Weisel[3,4,†]

[1]*King Fahd University of Petroleum and Minerals, Dhahran, Saudi Arabia*
[2]*CEA, DAM, DIF, F-91297 Arpajon, France*
[3]*Department of Physics, Duke University, Durham, North Carolina 27708 and Triangle Universities Nuclear Laboratory,*
Durham, North Carolina 27708, USA
[4]*Penn State Altoona, Altoona, Pennsylvania 16601, USA*
(Received 19 June 2012; published 10 September 2012)

Background: The nucleon-nucleus dispersive optical model (DOM) has been successful in providing good fits to scattering data and in making valuable predictions for bound-state properties in single- and double-closed shell nuclei. However, the generalizability of the DOM remains an ongoing issue.

Purpose: We investigate the DOM in the continuum and bound-state regions of the open-shell, self-conjugate nuclei ^{28}Si and ^{32}S. We collect new differential cross section and analyzing power data for elastic scattering at incident neutron energies between 8.0 and 18.9 MeV.

Methods: The measurements were conducted using a pulsed deuteron beam, the ^{2}He$(d,n)^{3}$He source reaction, and time-of-flight techniques. All data were corrected for finite-geometry effects. Phenomenological DOM potentials were tailored to fit the differential and total cross section data, and then extrapolated to the bound-state regions. The DOM bound-state predictions were then compared to experimental data available for single-particle energies, occupation probabilities, root-mean-square radii, and spectroscopic factors.

Results: The DOM bound-state predictions are in only fair agreement with experimental data and with USD shell-model predictions. Similar results are found after converting our neutron DOMs into proton DOMs. We investigate the separate effects of the dispersive surface and volume potential components on occupation probability and find that the volume component leads to a uniform depletion of the hole states, while the surface component acts mainly to deplete the valence orbitals. We compare these results to those of a variational multiparticle multihole configuration mixing (*mp-mh* CM) calculation using the Gogny D1S effective force.

Conclusions: We find that the phenomenological DOM, which was originally designed for spherical nuclei, show certain deficiencies when applied to open-shell nuclei and suggest possible avenues of improvement. We also find that the predictions of occupation probability by the DOM using the dispersive surface component are similar to those by the *mp-mh* CM. This lends support to the interpretation that the surface absorption in the optical model originates from particle-vibration couplings, that is, long-range correlations.

I. INTRODUCTION

For over 60 years, the nuclear optical model (OM) has provided a means of analyzing nuclear scattering data, both to characterize the nucleon-nucleus interaction and to represent nuclear data for applications in other research and in engineering [1]. Some of the most challenging nuclei to model have been those, such as ^{28}Si and ^{32}S, with relatively low atomic number and nonspherical properties. The Triangle Universities Nuclear Laboratory (TUNL) has made a dedicated study of neutron scattering from light nuclei to determine the limits of the OM approach. The present high-precision measurements of differential cross section, $\sigma(\theta)$, and analyzing power, $A_y(\theta)$, for elastic scattering complement data previously taken by TUNL. For ^{28}Si(n,n), we report on $\sigma(\theta)$ at $E_n = 15.4$ and 18.9 MeV and $A_y(\theta)$ at 15.4 and 18.6 MeV. For ^{32}S(n,n), we

report on $\sigma(\theta)$ at seven energies from 8.0 to 18.9 MeV and $A_y(\theta)$ at four energies from 9.9 to 16.9 MeV.

Our study investigates the limits of a specific type of OM, the dispersive optical model (DOM) of Mahaux and Sartor [2]. One benefit of the DOM is that it uses a dispersion relation linking the imaginary and real parts of the OM potential, which introduces a nonlinear energy dependence to the real strengths that is more detailed and physical than those of traditional OMs. Another is that the DOM simultaneously describes the positive-energy scattering regime and the negative-energy bound-state regime with a single, unified potential.

In recent years DOM studies have experienced a new impetus, with a focus placed on the asymmetry dependence of nucleon correlations in stable single- and double-closed shell nuclei spanning the $40 < A < 208$ mass region [3–5]. By using many-body Green's function methods, these recent DOM studies conclude that the surface-imaginary potential is associated with long-range correlations (LRCs), while the volume-imaginary potential is associated with short-range correlations (SRCs). Correlations have specific effects on

---

*jean-paul.delaroche@cea.fr
†gxw20@psu.edu

the bound-state quantities, particularly on the occupation probabilities, N_{nlj}, and spectroscopic factors, S_{nlj}, of the nucleon orbitals. LRCs originate from coupling between the nucleons of the independent particle model and the collective excitations of a nucleus [6,7], namely vibrations in spherical nuclei and collective excitations in open-shell nuclei (rotational and vibrational). Theory and DOM calculations for spherical nuclei indicate that LRCs smear out the Fermi sea and lead to significant quenching of the S_{nlj} for valence orbitals [6]. SRCs stem from the short-range nature and tensor component of the bare nucleon-nucleon force and manifest through the presence of strongly correlated pairs in nuclei [8]. Evidence for SRC effects in DOM calculations is rooted in the $1s_{1/2}$ proton occupation probabilities of Ca isotopes, which take on values close to $N_{nlj} = 0.90$ [5]. The fact that similar N_{nlj} values have been calculated for $1s_{1/2}$ neutron orbitals through the same isotopic chain, and also for the $1s_{1/2}$ proton level in ^{208}Pb, suggests that SRC effects on the N_{nlj} of the deepest nucleon orbitals of spherical nuclei do not significantly depend upon nuclear mass.

The present study explores the predictive power of the DOM in the continuum and bound-state regions for the open-shell nuclei ^{28}Si and ^{32}S. Of course, we do not expect perfect agreement between the DOM predictions and data. Both nuclei are deformed in their ground states (displaying oblate and prolate shapes, respectively, in the intrinsic reference frame) and feature rotational states in their excitation spectra. Our DOM analyses neglect the coupling between the ground states and the collective states. From previous scattering studies, it is known that the phenomenological OM does not account for certain effects of channel coupling onto the modulus of the matrix elements, especially for low partial waves [9].

After establishing our two DOMs by fitting separately the ^{28}Si and ^{32}S scattering databases (including our new data), we extrapolate the DOM predictions to the bound-state region, following the standard method exemplified by Ref. [10]. Because the reliability of DOM predictions for the bound-state properties of open-shell nuclei is *terra incognita*, we perform comparisons with measured bound-state quantities and with the predictions of the universal *s-d* (USD) shell model [11], obtained using the ANTOINE computer code [12]. It is well known that the USD shell model is successful in the interpretation of N_{nlj} and S_{nlj} measured for a number of *s-d* shell nuclei [13,14]. We also extend our DOMs to make similar comparisons for proton bound states, by using an approximation useful for self-conjugate nuclei [15].

To help disentangle the interplay between LRC and SRC effects in the DOM, we complement our study with two specific tests of the prediction of N_{nlj}. For the first, we generate a series of DOM variants in which different parts of the potential are turned off. For the second, we use the multiparticle, multihole configuration mixing (*mp-mh* CM) calculations of Pillet and co-workers [16,17], a microscopic model that is implemented with the finite-range, density-dependent Gogny D1S effective force [18]. The model is used to calculate the N_{nlj} for nucleons in ^{28}Si and ^{32}S to estimate the hole-orbital depletions originating from LRC effects.

The present paper is organized as follows. Section II reviews our experimental setup and data analysis for the $\sigma(\theta)$ and $A_y(\theta)$ data. Section III presents our database and standard OM analyses, elements of the DOM formalism, and DOM scattering predictions. Section IV presents our study of the bound-state region, including discussions of the DOM and *mp-mh* CM calculations and results, and the roles played by SRCs and LRCs. Finally, Sec. V provides a summary of the present work and makes several suggestions for extending DOM formalism to deformed, open-shell nuclei.

II. EXPERIMENTAL TECHNIQUES

A. Differential cross section

Our measurement of $\sigma(\theta)$ was performed for $E_n = 15.4$ and 18.9 MeV using the ^{28}Si target and $E_n = 8.0$, 9.9, 11.9, 13.9, 15.4, 16.9, and 18.9 MeV using the ^{32}S target. TUNL's beam handling, placement of detectors, and TOF target room have been described in earlier publications [19] and only a brief review will be given here. A deuteron beam was produced by TUNL's Direct-Extraction Negative Ion Source and then pulsed at 2.5 MHz. After exiting a FN Tandem Van de Graaff accelerator, the beam was bent by an analyzing magnet through 38° and transported to the time-of-flight (TOF) experimental area, where it entered a gas cell containing deuterium to produce neutrons via the ^{2}H(d, n)^{3}He reaction at 0°. The gas cell is a cylindrical tube of stainless steel (0.80 cm in diameter and 3.16 cm long) and lined with tantalum. On the beam-entrance side, the gas was contained with a 6.35-μm-thick Havar foil. The gas pressures depended on the incident neutron energy. As a typical example, for $E_n = 15.4$ MeV, we used a pressure of 4.0 atm, resulting in a beam energy spread of 160 keV.

Four cylindrical scattering samples were used. The ^{28}Si sample (92.55% natural abundance) had a radius of 1.176 cm, and a height of 2.528 cm, while the ^{32}S sample (95.28%) had a radius of 1.230 cm, and a height of 2.540 cm. In addition, a polyethylene (CH$_2$) and a ^{12}C scatterer were used for the purpose of absolute normalization. All four samples were mounted on a vertical steel wire, at a center-to-center distance from the gas cell of typically 12 cm.

The scattered neutrons were detected using the TUNL TOF spectrometer, which includes four cylindrical detectors (either NE-213 or NE-218 liquid organic scintillators coupled to photomultiplier tubes). Two side detectors were located in the horizontal plane to the right and left of the incident beam axis. The right detector has a diameter of 8.88 cm, and a thickness of 5.08 cm and was set at distances from the target ranging from 2.5 to 3.9 m. The left detector has a diameter of 12.7 cm and a thickness of 5.08 cm and was set at distances ranging from 3.8 to 5.7 m. Both are heavily shielded with paraffin and lithium carbonate and use tungsten shadow bars to shield against the direct neutron flux. The third detector, the ceiling monitor, monitored the neutron flux from the gas cell. It was 5.1 cm in diameter and 5.1 cm in thickness and was mounted at a distance of 1.8 m above the reaction plane at an angle of about 50° and housed in a 50-kg copper cylinder. The location and collimation of this detector serve to reduce its illumination

by neutrons scattered from the scattering samples and the shielding in the reaction plane. We drew a linear background in the ceiling monitor's TOF spectrum, by fitting regions on either side of the mono-energetic neutron peak. A fourth detector, the zero-degree monitor, located about 4 m downstream of the gas cell, was used to monitor the beam's time characteristics; full width at half maximum of the beam bursts was kept under 2 ns.

For the right, left, and ceiling detectors, a threshold was set on the recoil pulse height (at a level of $1 \times {}^{137}$Cs) to reject low-energy events. In addition, pulse-shape discrimination was used to differentiate between γ and neutron pulses. The neutron TOF was based on two signals, a start signal from the neutron detector and a delayed stop signal from the capacitive pickoff, located just upstream from the gas cell. Using this method, the dead-time corrections were negligible.

Data were accumulated with the left and right detectors at angles from $18°$ to $160°$ in steps of about $4°$. At each angle, two TOF spectra were collected: the "sample-in" condition, in which either the ^{28}Si or ^{32}S samples were placed in the neutron beam, and the "sample-out" condition, in which the sample was removed and replaced by a bare wire. To normalize the sample-out spectra, we set a window on the neutron peak of the ceiling monitor's TOF spectrum and then found its yields for sample-in (Y_{mon}^{in}) and sample-out (Y_{mon}^{out}). The sample-out spectra of the right and left detectors were then normalized by multiplying them by the ratio $Y_{mon}^{in}/Y_{mon}^{out}$.

To extract the neutron yields at each angle, "difference spectra" were generated by subtracting the sample-out spectra from the associated sample-in spectra. The difference spectra exhibited small residual backgrounds, which were well described by a linear fit. The "neutron yields per monitor," $Y_S(\theta)$, was found by subtracting the linear background from the difference spectrum and then dividing by the sample-in monitor yield, Y_{mon}^{in}. Periodically, normalization measurements were taken with the CH$_2$ and ^{12}C scatterers at scattering angle θ_H. The θ_H depended on the incident neutron energy; for the 15.4 MeV measurement, we used $\theta_H = 27°$. The yield per monitor for n-p scattering, $Y_H(\theta_H)$, was found by subtracting the ^{12}C spectrum from the CH$_2$ spectrum.

The measured differential cross sections, $\sigma(\theta, E_n)$, for the ^{28}Si and ^{32}S samples at the laboratory angle θ and neutron energy E_n were found using the equation

$$\sigma(\theta, E_n) = Y_S(\theta) \frac{\sigma(\theta_H, E_n)}{Y_H(\theta_H)} \frac{N_H}{N_S} \frac{1}{F(\theta_H, E_n)}, \qquad (1)$$

where $\sigma(\theta_H, E_n)$ is the n-p cross section and N_H/N_S is the number of hydrogen nuclei in the CH$_2$ sample divided by the number of nuclei in the scattering sample. The $F(\theta_H, E_n)$, a correction factor accounting for detector-efficiency and finite-geometry effects associated with n-p scattering, was found with a Monte Carlo simulation; at $E_n = 15.4$ MeV, it was 1.205.

Our data contained three finite-geometry effects: attenuation of the neutron flux in the target, multiple scattering in the target (double and triple), and variation of $\sigma(\theta)$ for the source reaction and for neutron-nucleus elastic scattering across the face of the scattering elements. All three effects were removed from the $\sigma(\theta)$ data using a standard iterative procedure and the

Monte Carlo code EFFIGY [20]. This procedure entailed angle shifts of less than $1°$, except on the steep slopes of the angular distribution were it reached up to $2.3°$. The simulation also calculated the mean neutron energies.

The uncertainties for the $\sigma(\theta)$ data include seven sources. Three are relative uncertainties, added in quadrature, owing to the counting statistics and background determination (ranging from 1.5% to 6.0%), the relative detector efficiency (2.5%), and the finite-geometry corrections (from 0.8 to 1%). Four more are scale uncertainties, owing to the n-p yield (0.5 to 1.0%), the n-p cross section (2.0%), the N_H/N_S factor (0.8 to 1%), and the $F(\theta_H, E_n)$ factor (2.2%). Figures 1 and 2 display our final $\sigma(\theta)$ data as the red solid squares. The final uncertainties are typically 2% or lower, except in the minimum of the cross section, where they are as high as 6%.

B. Analyzing power

The $A_y(\theta)$ measurements proceeded similarly to those for $\sigma(\theta)$ but used a polarized ion source to produce a beam of polarized deuterons. Four of the measurements, ^{28}Si at $E_n = 18.6$ MeV and ^{32}S at 9.9, 13.9, and 16.9 MeV, used TUNL's Lamb-shift source, which monitored the beam polarization with a quench-ratio method. The other two $A_y(\theta)$ distributions at $E_n = 15.4$ MeV used TUNL's Atomic Beam Polarized Ion Source (ABPIS).

After the deuteron beam was pulsed and accelerated, it was bent through $38°$ and transported to the NTOF target area, where polarized neutrons were produced via the ^{2}H($\vec{d}, \vec{n}$)^{3}He reaction, using the same gas cell as that for the $\sigma(\theta)$ measurements. Because the polarized ion sources produce relatively low deuteron currents (about 450 nA with the ABPIS), we ran the gas cell at higher pressures to improve the counting rate. As a result, the energy spreads were higher, varying from 200 to 460 keV, depending on the measurement. The neutrons were detected by the right and left detectors, which were now positioned symmetrically about the beam axis. To cancel instrumental asymmetries (owing to the detectors and their associated electronics) the data were accumulated using the spin-flip method, in which the polarization of the incident neutron beam was periodically flipped up and down. For each angle, eight TOF spectra were accumulated, for right and left, for sample-in and sample-out, and for spin up and spin down. The neutron flux was no longer monitored with the ceiling monitor but with a beam-current integrator.

As with the $\sigma(\theta)$ measurements, difference spectra were generated by subtracting the sample-out spectra from the sample-in spectra. Again, a small residual background remained. Within statistical uncertainties, this background had the same level for both the spin-up and spin-down spectra and was well represented by a linear function; no evidence of a polarized background was found.

After the determination of the background, three windows were set on the elastic neutron peaks at 10%, 20%, and 50% of the peak height. For each case, yields were generated for R_U, R_D, L_U, and L_D, where R and L designate the right and left detectors, respectively, and U and D designate spin up and spin down, respectively. After defining the quantity
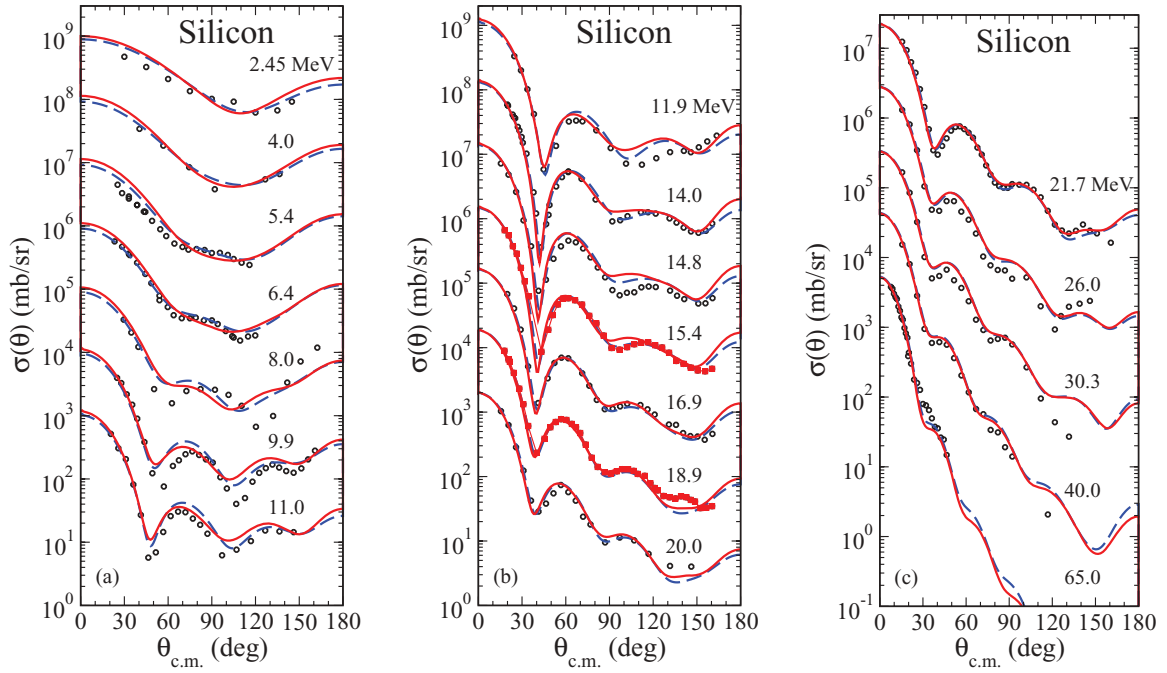
FIG. 1. (Color online) Differential cross sections, $\sigma(\theta)$, for silicon. The data of the present work are shown in panels (a), (b), and (c) as the red solid squares. The predictions are the Koning-Delaroche local OMs (blue dashed curves) and the current DOM (red curves). In each panel, the curves and data points at the bottom represent the true values, while the others are offset by factors of 10, 100, and so on.

$\alpha = \sqrt{\frac{L_U R_D}{R_U L_D}}$, the analyzing power is

$$A_y(\theta) = \frac{1}{P_n} \frac{\alpha - 1}{\alpha + 1}. \tag{2}$$

For the 15.4-MeV measurements, the neutron beam polarization, P_n, was monitored by using the $^{12}C(n,n)$ reaction. Approximately every 8 h during the experiment, the right and left detectors were positioned at $\theta_{\text{lab}} = 50°$, with the ^{12}C scatterer used for the sample-in position. Using the known $^{12}C(n,n)$ $A_y(\theta)$ value from Ref. [21], Eq. (2) was inverted to find P_n (typically 55%).
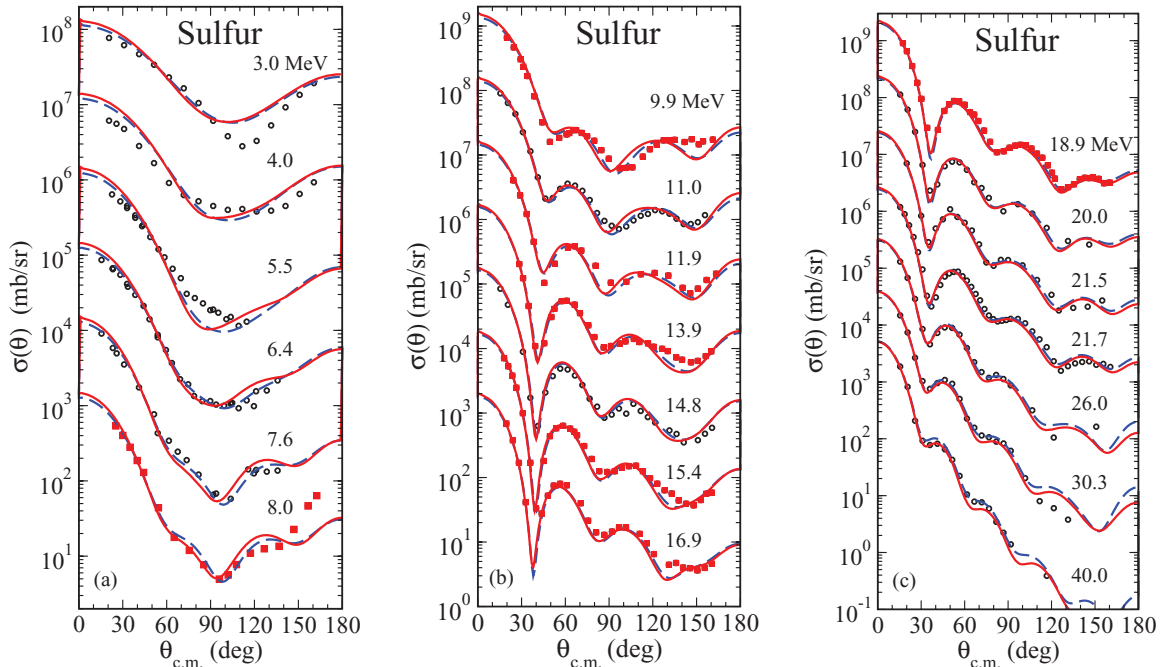

FIG. 2. (Color online) Differential cross sections, $\sigma(\theta)$, for sulfur. For details, see the caption of Fig. 1.
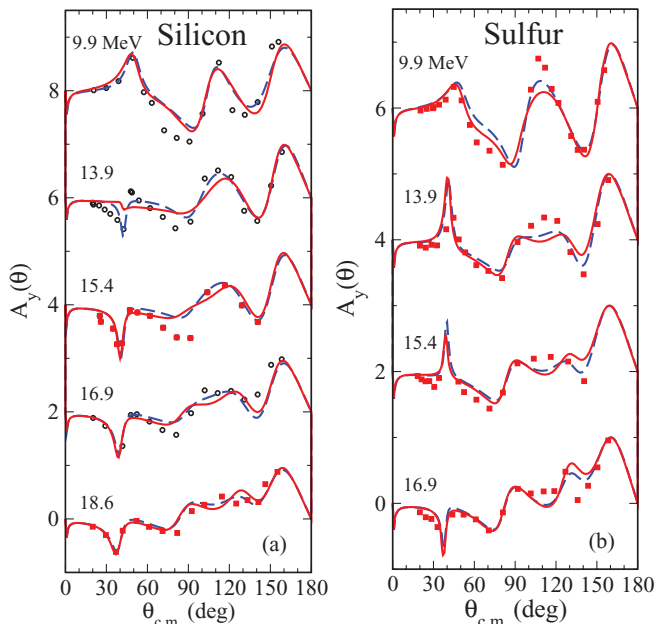
FIG. 3. (Color online) Analyzing powers, $A_y(\theta)$, for silicon [panel (a)] and sulfur [panel (b)]. The data of the present work are shown as the red solid squares. The predictions are the Koning-Delaroche local OMs (blue dashed curves) and the current DOMs (red curves). In both panels, the curves and data points at the bottom represent the true values, while the others are offset by factors of 2, 4, and so on.

We found that the $A_y(\theta)$ results were consistent within uncertainties for all three choices of gates (10%, 20%, and 50%), indicating that the background was defined reliably. The 20% gates were used for the final data, because they represented a good tradeoff between maximizing the neutron yields and eliminating unwanted counts. We corrected the $A_y(\theta)$ data for effects of finite geometry, flux attenuation, and multiple scattering using the Monte Carlo code JANE [22], which also calculated the mean neutron energies.

The ^{28}Si and ^{32}S $A_y(\theta)$ data have relative uncertainties ranging between 2% (at the forward angles) and 7% (near the minima). These relative uncertainties include the statistical uncertainties, the uncertainties associated with background subtraction, and those owing to the finite-geometry corrections, all added in quadrature. In addition, we folded in two scale uncertainties: a 2% uncertainty in the determination of the deuteron beam polarization and a 5% uncertainty assigned to the analyzing power of ^{12}C(n,n). Figure 3 displays our final $A_y(\theta)$ data as the red solid squares.

III. SCATTERING MODEL ANALYSES

A. Database and standard OM analysis

The ^{28}Si database, listed in Table I, included 40 data points for total cross section based on Refs. [23,24]. We used 17 $\sigma(\theta)$ angular distributions from Refs. [25–31] along with the present data at 15.4 and 18.9 MeV. We also used three $A_y(\theta)$ distributions from Ref. [27] and the present data at 15.4 and 18.6 MeV. The ^{32}S(n,n) database, listed in Table II, included 40 data points of total cross section based on Refs. [23,32].

TABLE I. The silicon database used to develop the DOM.

Parameter	Energy (MeV)	Reference
$\sigma(\theta)$	2.45, 4.0	[25]
	5.4, 6.4	[26]
	8.0, 9.9, 11.9, 14.0, 16.9	[27]
	11.0, 20.0, 21.7, 26.0	[28]
	14.8	[29]
	15.4, 18.9	Present work
	30.3, 40.0	[30]
	65.0	[31]
$A_y(\theta)$	9.9, 13.9, 16.9	[27]
	15.4, 18.6	Present work
σ_T	0.5–5	[23]
	5–160	[24]

It also used 13 $\sigma(\theta)$ angular distributions from Refs. [28,29, 33–37] and the present $\sigma(\theta)$ data at 8.0, 9.9, 11.9, 13.9, 15.4, 16.9, and 18.9 MeV. Finally, it included the present $A_y(\theta)$ data at 9.9, 13.9, 15.4, and 16.9 MeV. Traditionally, TUNL OM studies went up to 80 MeV. However, owing to improvements in the nuclear database, particularly for total cross section, the present study goes up to 160 MeV.

As a preliminary step, we compared our data to the predictions of the Koning-Delaroche (KD) global OM [38], which covers many target nuclides in the mass range from $A = 24$ to 209 for incident neutrons and protons up to 200 MeV. The KD OM uses a standard form for the potential

$$
\begin{aligned}
U(r, E) = &-[V_V(E) + iW_V(E)] f(r, R_V, a_V) \\
&- 4a_D [V_D(E) + iW_D(E)] \frac{d}{dr} f(r, R_D, a_D) \\
&- \bar\lambda_\pi^2 [V_{SO}(E) + iW_{SO}(E)] \frac{1}{r} \frac{d}{dr} f(r, R_{SO}, a_{SO}) \\
&\times (l \cdot \sigma),
\end{aligned} \tag{3}
$$

where the successive complex-valued terms are the volume-central, surface-central, and spin-orbit potentials. The $f(r, R_i, a_i)$ is the Woods-Saxon form factor. The predictions of this global OM are confirmed nicely by our data, as shown by the blue dashed curves in Figs. 1 to 4.

TABLE II. The sulfur database used to develop the DOM.

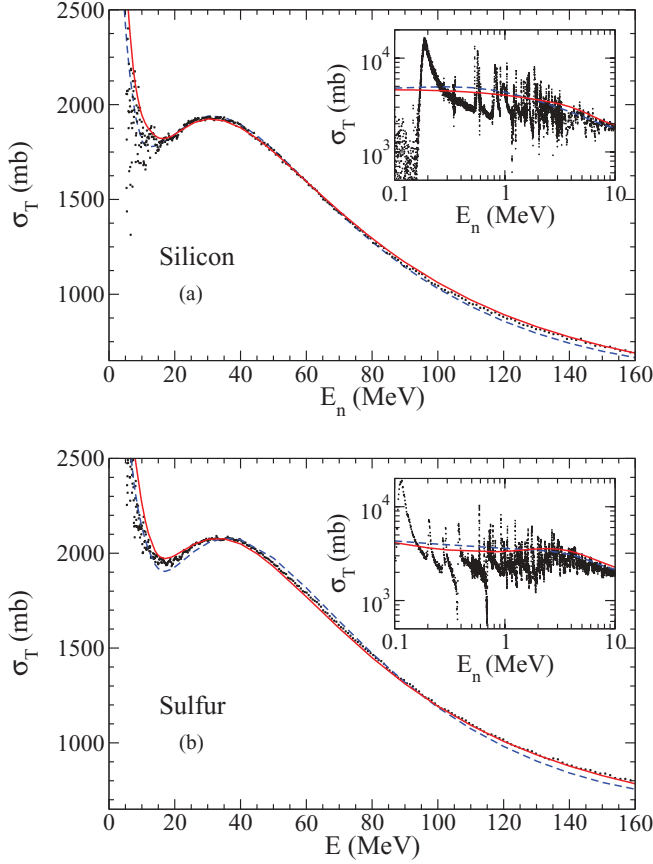| Parameter	Energy (MeV)	Reference
$\sigma(\theta)$	3.0, 4.0	[33]
	5.5, 6.4, 7.6	[34]
	8.0, 9.9, 11.9, 13.9, 15.4, 16.9, 18.9	Present work
	11.0	[35]
	14.8	[29]
	20.0, 21.7, 26.0	[28]
	21.5	[36]
	30.3, 40.0	[37]
$A_y(\theta)$	9.9, 13.9, 15.4, 16.9	Present work
σ_T	0.5–5	[23]
	5–160	[32]

FIG. 4. (Color online) Neutron total cross sections, σ_T, for silicon [panel (a)] and sulfur [panel (b)]. Experimental data are shown as black dots. The predictions are the Koning-Delaroche local OMs (blue dashed curves) and the current DOMs (red curves).

The silicon database includes $\sigma(\theta)$ data at 65 MeV [31]. These measurements were performed with an energy resolution of $\Delta E = 2.7$ MeV [39], making it impossible to separate scattering from the ground state and from the first 2^+ excited state at $E_x = 1.779$ MeV. Therefore, we made an estimate of the inelastic scattering angular distribution at this incident energy, performing a DWBA calculation (using the KD potential) and a quadrupole deformation parameter inferred from a neutron inelastic scattering analysis for ^{28}Si [40]. The same method, using ECIS94 [41], was used with success in Ref. [42]. The DWBA results were summed with those for elastic scattering using the KD and DOM potentials. The two curves for 65 MeV in panel (c) of Fig. 1 are for this sum. At the forward angles, the inelastic contribution is smaller than the uncertainties on the data. In the $30°$–$50°$ range it raises the predictions slightly closer to the measurements.

B. Dispersive optical model formalism

The DOM potential strengths include a real-valued Hartree-Fock mean field (V_{HF}), an imaginary potential with both volume and surface terms (W_V and W_D, respectively), volume and surface dispersive corrections to the real potential (ΔV_V and ΔV_D, respectively), and a real spin-orbit term (V_{SO}). With the

radial dependencies, the general form of the DOM potential is

$$U(r, E) = -[V_{HF}(E) + iW_V(E) + \Delta V_V(E)]\, f(r, R_V, a_V)$$
$$- 4a_D\,[iW_D(E) + \Delta V_D(E)]\,\frac{d}{dr}f(r, R_D, a_D)$$
$$- \lambda_\pi^2\, V_{SO}(E)\frac{1}{r}\frac{d}{dr}f(r, R_{SO}, a_{SO})(l \cdot \sigma). \quad (4)$$

The volume and surface dispersive terms are computed with the integral

$$\Delta\mathcal{V}_i(r, E) = \frac{1}{\pi}P\int_{-\infty}^{+\infty}\frac{\mathcal{W}_i(r, E')}{E' - E}dE', \quad (5)$$

where P stands for the principal value, $\mathcal{W}$ stands for the absorptive parts of Eq. (4), and the subscript "i" is for either volume (V) or surface (D) components. We did not use an imaginary spin-orbit term for our DOM analyses, because a number of earlier TUNL studies did not show a need for a W_{SO}, especially at low energies [43].

The energy dependence of the volume imaginary potential depth is assumed to be of the form

$$W_V(E) = \frac{w_1(E - E_F)^2}{(E - E_F)^2 + (w_2)^2}, \quad (6)$$

while that for the surface imaginary potential is

$$W_D(E) = \frac{d_1(E - E_F)^2}{(E - E_F)^2 + (d_3)^2}\exp[-d_2(E - E_F)]. \quad (7)$$

The W_V and W_D terms are assumed to be symmetric around the Fermi energy, E_F, which is evaluated in terms of neutron separation energies, S_n, as $E_F = \frac{1}{2}[S_n(N) + S_n(N + 1)]$. For ^{28}Si, $E_F = -12.83$ MeV and for ^{32}S, $E_F = -11.84$ MeV. We did not follow Refs. [4,5] in using a form of W_V that is asymmetric about E_F.

We considered two forms for the energy dependence of the Hartree-Fock potential, V_{HF}. The first is the traditional single-exponential energy dependence,

$$V_{HF}(E) = v_{hf1}\exp[-v_{hf2}(E - E_F)]. \quad (8)$$

The second is used by Ref. [4] and employs two exponential terms

$$V_{HF}(E) = v_{hf1}\exp[-v_{hf2}(E - E_F)]$$
$$+ v_{hf3}\exp[-v_{hf4}(E - E_F)]. \quad (9)$$

Both forms comply with the usual assumption introduced by Mahaux and Sartor [2], according to which the HF potential uses an energy dependence that is smooth and monotonic and an energy-independent radial form factor. Equation (8) provides a simple on-shell representation of the Perey-Buck nonlocal potential, where the nonlocality profile is of the Gaussian type [2,44,45].

C. DOM scattering results

The strength and geometry parameters for the present ^{28}Si(n,n) and ^{32}S(n,n) DOMs are displayed in Table III. In building our DOMs we started with the volume- and surface-imaginary potentials (W_V and W_D, respectively) of the "best" models of Ref. [38] and then calculated the

TABLE III. DOM potential parameters for the two scattering systems. Energies and potential depths are in MeV. Geometries are in fm.

$n + ^{28}$Si			
$v_{hf1} = 56.0;$	$v_{hf2} = 0.009\,10;$	$E_F = -12.83$	
$w_1 = 14.0;$	$w_2 = 70.0;$	$r_V = 1.23;$	$a_V = 0.690$
$d_1 = 13.6;$	$d_2 = 0.0216$		
	$d_3 = 11.1;$	$r_D = 1.29;$	$a_D = 0.530$
$v_{so1} = 6.00;$	$v_{so2} = 0.0040;$	$r_{SO} = 1.00;$	$a_{SO} = 0.580$
$n + ^{32}$S			
$v_{hf1} = 54.0;$	$v_{hf2} = 0.009\,50;$	$E_F = -11.84$	
$w_1 = 14.0;$	$w_2 = 70.0;$	$r_V = 1.26;$	$a_V = 0.690$
$d_1 = 15.2;$	$d_2 = 0.0216$		
	$d_3 = 11.1;$	$r_D = 1.34;$	$a_D = 0.530$
$v_{so1} = 6.00;$	$v_{so2} = 0.0040;$	$r_{SO} = 1.00;$	$a_{SO} = 0.580$

volume and surface dispersive corrections, ΔV_V and ΔV_D, respectively, using Eq. (5). We made small adjustments to the W_V and W_D parameters, but found that large changes spoiled the fits to the differential data. For the real spin-orbit potential, we used the form of Ref. [38],

$$V_{SO}(E) = v_{SO1} \exp\left[-v_{SO2}(E - E_F)\right]. \tag{10}$$

We then determined the Hartree-Fock term, $V_{HF}(E)$. After first finding V_{HF} values that reproduced σ_T at each E_n, we fit these values using the single-exponential form Eq. (8). Local stepping of the strength, slope, and geometry resulted in a fairly good representation of σ_T, as shown by the red curves in Fig. 4.

The DOM faced a tradeoff between the low- and high-energy regimes of σ_T. Because our database included high-precision data between 25 and 160 MeV from Refs. [24,32], we gave special attention to this region, achieving as good or better fits (red curves) than those of Ref. [38] (blue dashed). As a result, our DOM fits are not as good in the low-energy regime (from $E_n = 0$ to 25 MeV), where they are somewhat higher than the data. Use of the double-exponential form of Eq. (9) did not cure this weakness but, on the contrary, exacerbated the problem because it features higher $V_{HF}(E)$ slopes at low energies, whereas the σ_T data call for lower slopes. In separate tests, we found that the low-energy fits could be greatly improved by using an energy-dependent r_V. For the ^{28}Si DOM, r_V changed value linearly from 1.18 to 1.23 fm between 0 to 25 MeV, after which it was constant at 1.23 fm. Similarly, for the ^{32}S DOM, r_V rose from 1.21 to 1.26 fm between 0 and 25 MeV and then was constant at 1.26 fm. Although this exercise confirmed that the DOM potentials were too strong at low energy, we rejected the modification because it introduced two new parameters.

Comparisons are shown between the predictions of the DOMs (red curves) and data for $\sigma(\theta)$ in Figs. 1 and 2 and for $A_y(\theta)$ in Fig. 3. All of our scattering calculations included the Mott-Schwinger interaction and relativistic kinematics. We accounted for compound nucleus (CN) processes below 12 MeV for both targets, using the TALYS computer code [46]. All open channels (n, p, d, t, α) were treated and width fluctuation factors were calculated according to Ref. [47]. In displaying

the OM predictions of differential observables, we added the CN contributions to each $\sigma(\theta)$ prediction below 12 MeV and applied the appropriate ratio to the 9.9 MeV $A_y(\theta)$ predictions.

In the higher-energy regime where our models give good predictions for σ_T, they also give good predictions for differential scattering quantities. In the low-energy regime, the present fits to $\sigma(\theta)$ are too high (especially at forward scattering angles), reflecting the fact that the predictions for σ_T are too high. The predictions of the traditional global OM of Ref. [38] (blue dashed curves) do not have this deficiency. It appears that the additional potential strength introduced by the DOM formalism at low energies has made it difficult to find a $V_{HF}(E)$ representation that satisfies both the low- and high-energy regimes. Note that our fit to the ^{28}Si $A_y(\theta)$ data at 13.9 MeV misses for angles less than 90° and does not do as well as the predictions of Ref. [38]. This does not indicate a problem with the spin-orbit interaction but rather is related to the difficulty we had in fitting the σ_T minimum in the 0- to 25-MeV regime.

The tradeoff between the low- and high-energy regimes affected the low-energy predictions of σ_T and $\sigma(\theta)$ and other low-energy parameters as well. The s- and p-wave strength functions, S_0 and S_1, respectively, are determined in Ref. [48] by averaging resonance parameters over a few hundred keV. For $n + ^{32}$S, Ref. [48] gives $S_0 = (0.73 \pm 0.23) \times 10^{-4}$ and $S_1 = (0.57 \pm 0.14) \times 10^{-4}$, while our DOM yields $S_0 = 1.14 \times 10^{-4}$ and $S_1 = 1.85 \times 10^{-4}$. Also, Ref. [48] gives the potential scattering radius as $R' = 3.92 \pm 0.02$ fm, while our DOM yields 3.41 fm.

Our scattering fits show deficiencies in certain energy and angle regimes, as do our prediction of the s and p wave strengths. In these regards, the DOM shares many deficiencies (and possible ways of rectifying them) with the standard OM. A number of earlier studies have indicated that the predictions of phenomenological OMs can be improved by using l- and parity-dependent potential terms [49]. Another possibility is that similar effects can be accounted for with coupled-channel calculations. For example, OM studies of neutron scattering from ^{32}S and related targets by MacKellar and co-workers found that deficiencies in the s- and p-wave strength function calculations based on a spherical OM could be cured dynamically when deformations of the target nuclei are introduced [50].

IV. BOUND-STATE MODEL ANALYSES

A. DOM at negative energies

After establishing best fits to the continuum database, a crucial test of the DOM is to see how well it predicts the bound-state centroid energy, E_{nlj}, occupation probability, N_{nlj}, root-mean-square radius, R_{nlj}^{rms}, and spectroscopic factor, S_{nlj}. The E_{nlj} are the eigenvalues of the wave equation

$$\left[-\frac{\hbar^2}{2m}\nabla^2 + \mathcal{V}(r; E_{nlj})\right]\Phi_{nlj} = E_{nlj}\Phi_{nlj}, \tag{11}$$

with quantum numbers n, l, and j. For neutron bound states, the nuclear potential, $\mathcal{V}(r; E_{nlj})$, includes contributions from the Hartree-Fock potential (V_{HF}), the two dispersive corrections (ΔV_V and ΔV_D), and the spin-orbit interaction

(V_{SO}). Following the prescription of Ref. [44], for $E < E_F$, the V_{HF}, was extrapolated linearly, using the slope of Eq. (8) at $E = E_F$. Using this potential, we calculated the bound-state quantities with software originally written by Johnson [51].

It is convenient to define two effective masses, the first being the momentum-dependent effective mass (or k mass),

$$\frac{m^*_{HF}(r, E)}{m} = 1 - \frac{d\mathcal{V}_{HF}(r, E)}{dE}, \tag{12}$$

and the second the energy-dependent effective mass (or E mass),

$$\frac{\overline{m}(r, E)}{m} = 1 - \frac{m}{m^*_{HF}(r, E)} \frac{d\Delta\mathcal{V}(r, E)}{dE}. \tag{13}$$

The R^{rms}_{nlj} were computed using the equation

$$R^{rms}_{nlj} = \sqrt{\int_0^{+\infty} \overline{u}^2_{nlj}(r) r^2 dr}. \tag{14}$$

The $\overline{u}_{nlj}(r)$ are the radial parts of the Φ_{nlj} wave functions, which have been corrected for nonlocality according to

$$\overline{u}_{nlj} = \sqrt{\frac{m^*_{HF}(r, E)}{m}} u_{nlj} \tag{15}$$

and which have been normalized. The N_{nlj} were computed for hole states using

$$N_{nlj} = \int_0^{+\infty} \overline{u}^2_{nlj}(r) \left[1 + \frac{m}{m^*_{HF}(r, E_{nlj})} \right.$$
$$\left. \times \frac{1}{\pi} \int_{E_F}^{+\infty} \frac{\mathcal{W}_i(r, E')}{(E' - E_{nlj})^2} dE' \right] dr \tag{16}$$

and for particle states using

$$N_{nlj} = -\int_0^{+\infty} \overline{u}^2_{nlj}(r)$$
$$\times \left[\frac{m}{m^*_{HF}(r, E_{nlj})} \frac{1}{\pi} \int_{-\infty}^{E_F} \frac{\mathcal{W}_i(r, E')}{(E' - E_{nlj})^2} dE' \right] dr. \tag{17}$$

Finally, the S_{nlj}, relative to the independent-particle values, were computed using

$$S_{nlj} = \int_0^{+\infty} \overline{u}^2_{nlj}(r) \frac{m}{\overline{m}(r, E_{nlj})} dr. \tag{18}$$

Equations (16)–(18) rely upon approximations introduced in Ref. [2] and discussed in Ref. [5]. The results of our bound-state calculations are listed in Tables IV and V, and are discussed in Sec. IV C.

B. Multiparticle, multihole configuration mixing calculations

We use a beyond-mean-field method based on *mp-mh* CM to estimate the orbital depletions arising from LRCs. This microscopic approach aims to unify nuclear LRCs in a symmetry-preserving framework [16,17]. The trial wave function, $|\Psi\rangle$, is built as a superposition of Slater determinants,

$$|\Psi\rangle = \sum_{\alpha_\nu, \alpha_\pi} A_{\alpha_\nu, \alpha_\pi} \left[|\Phi_{\alpha_\nu}\rangle \otimes |\Phi_{\alpha_\pi}\rangle \right], \tag{19}$$

TABLE IV. Neutron bound-state properties. The middle columns show DOM predictions of binding energy, E_{nlj}, compared to experimental data [52]. Values for pairs of nonresolved states are shown with a double arrow linking them. The right columns show DOM predictions of occupation probabilities, N_{nlj}, compared to experimental data [53,54] and predictions of the USD shell model and the *mp-mh* CM calculations.

State		$-E_{nlj}$ (MeV)		N_{nlj}			
		DOM	Exp.	DOM	Exp.	USD	CM
^{28}Si	$1f_{7/2}$	2.29	—	0.116	0.010	—	0.055
	$1d_{3/2}$	9.67	—	0.228	0.255	0.168	0.074
	$2s_{1/2}$	11.8		0.283	0.400	0.352	0.166
	$\updownarrow$		17(3)				
	$1d_{5/2}$	14.6		0.713	0.717	0.770	0.885
	$1p_{1/2}$	25.6		0.868	—	—	0.932
	$\updownarrow$		32(6)				
	$1p_{3/2}$	32.2		0.893	—	—	0.954
	$1s_{1/2}$	51.9	52(15)	0.923	—	—	0.970
^{32}S	$1f_{7/2}$	6.09	—	0.186	—	—	0.059
	$1d_{3/2}$	11.4	—	0.378	0.175	0.290	0.109
	$2s_{1/2}$	13.1	—	0.699	0.650	0.709	0.922
	$1d_{5/2}$	16.7	—	0.790	1.000	0.903	0.921
	$1p_{1/2}$	28.8	—	0.883	—	—	0.939
	$1p_{3/2}$	35.2	—	0.901	—	—	0.968
	$1s_{1/2}$	53.2	—	0.924	—	—	0.986

where the $A_{\alpha_\nu, \alpha_\pi}$ represent a set of mixing coefficients and the $|\Phi_{\alpha_\pi}\rangle$ and $|\Phi_{\alpha_\nu}\rangle$ the proton and neutron Slater determinants, respectively. As seen from Eq. (19), the proton-proton, proton-neutron, and neutron-neutron correlations are treated on the same ground.

Both mixing coefficients and single-particle orbitals $|\varphi_i\rangle$ are unknown quantities. They are determined by applying a variational principle to the energy functional $\mathcal{F}(\rho)$ defined as

$$\mathcal{F}(\rho) = \langle\Psi|\hat{H}(\rho)|\Psi\rangle - \lambda\langle\Psi|\Psi\rangle, \tag{20}$$

where ρ is the one-body density matrix. The Hamiltonian $\hat{H}(\rho) = \hat{T} + \hat{V}(\rho)$, where $\hat{V}(\rho)$ represents the two-body density-dependent Gogny D1S effective force plus the Coulomb term. Moreover, $\hat{T}$ and $\hat{V}(\rho)$ contain one- and two-body center-of-mass corrections, respectively. The minimization of the energy functional, namely $\delta[\mathcal{F}(\rho)] = 0$, leads to

$$\frac{\partial\mathcal{F}(\rho)}{\partial A^*_{\alpha_\nu\alpha_\pi}} = 0 \quad \text{and} \quad \frac{\partial\mathcal{F}(\rho)}{\partial\varphi^*_i} = 0. \tag{21}$$

The set of equations Eq. (21) may be re-expressed as a set of nonlinear equations,

$$\sum_{\alpha'_\pi\alpha'_\nu} \mathcal{H}_{\alpha_\pi\alpha_\nu, \alpha'_\pi\alpha'_\nu} A_{\alpha'_\pi\alpha'_\nu} = \lambda A_{\alpha_\pi\alpha_\nu}, \tag{22}$$

and inhomogeneous Hartree-Fock (HF) equations

$$[h(\rho, \sigma), \rho] = G(\sigma). \tag{23}$$

In Eq. (22), $\mathcal{H}$ contains contributions from $\hat{H}(\rho)$ and rearrangement terms coming from the density-dependent part

TABLE V. Proton bound-state properties. The middle columns show DOM predictions of E_{nlj} compared to experimental data. The data listed in columns Exp. A and Exp. B are, for ^{28}Si, from Refs. [56] and [57,58], respectively, and, for ^{32}S, from Refs. [59] and [60], respectively. Values for pairs of nonresolved states are shown with a double arrow linking them and those marked with square brackets are considered tentative. The right columns show DOM predictions of N_{nlj} compared to experimental data [53,56,62] and predictions of the USD shell model and the *mp-mh* CM calculations. The notation "ub" stands for "unbound."

	State	$-E_{nlj}$ (MeV)			N_{nlj}			
		DOM	Exp. A	Exp. B	DOM	Exp.	USD	CM
^{28}Si	$1f_{7/2}$	ub	—	—	ub	—	—	0.054
	$1d_{3/2}$	4.04	—	1.36	0.222	0.247	0.168	0.072
	$2s_{1/2}$	6.12	—	2.75	0.270	0.395	0.352	0.163
	$1d_{5/2}$	8.72	16.1(8)	11.8(1)	0.707	0.703	0.770	0.888
	$1p_{1/2}$	18.9			0.863			0.933
	$\updownarrow$		[32]	27(2)				
	$1p_{3/2}$	25.5			0.890	—	—	0.955
	$1s_{1/2}$	44.4	[51]	47(4)	0.921	0.900	—	0.970
^{32}S	$1f_{7/2}$	0.22	—	—	0.186	0.014	—	0.057
	$1d_{3/2}$	5.12	—	—	0.373	0.150	0.290	0.106
	$2s_{1/2}$	6.76	9(3)		0.704	0.750	0.709	0.924
	$\updownarrow$			15(2)				
	$1d_{5/2}$	10.1	16(3)		0.785	0.983	0.903	0.923
	$1p_{1/2}$	21.4	[26.6]		0.879	—	—	0.940
	$\updownarrow$			44(7)				
	$1p_{3/2}$	27.8	[32.2]		0.898	—	—	0.969
	$1s_{1/2}$	44.9	—	72(9)	0.923	—	—	0.986

of the Gogny D1S effective force. In Eq. (23), h represents the one-body Hamiltonian deduced from $\hat{H}(\rho)$ and σ the two-body density matrix. Only Eqs. (22) are solved, in keeping with methodology adopted in a recent study of excited states in nuclei of the *sd*-mass region [17].

In the present work, the numerical procedure is as follows. The proton and neutron single-particle orbitals are obtained in HF calculations performed at sphericity. The HF equations are solved by expanding the solutions onto a harmonic oscillator basis including 11 major shells, which is large enough to ensure convergence of the results. The *mp-mh* configuration space is built by considering up to eight-particle–eight-hole excitations. The secular equation [Eq. (22)] is solved including neutron and proton levels $1s_{1/2}$, $1p_{3/2}$, $1p_{1/2}$, $1d_{5/2}$, $2s_{1/2}$, $1d_{3/2}$, and $1f_{7/2}$ as active orbitals. The ground-state solution, with angular and parity $J^\pi = 0^+$, that is, $|\Psi_{0+}\rangle$, is obtained using the Lanczos algorithm to diagonalize the matrices, which, in this case, included about 8×10^8 elements. Occupation probabilities are determined as $N_i = \langle \Psi_{0+} | a_i^+ a_i | \Psi_{0+} \rangle$, where a_i^+ is a single-particle creation operator for orbital i with quantum numbers n, l, and j. The N_{nlj} values resulting from the *mp-mh* CM calculations for ^{28}Si and ^{32}S are displayed in Tables IV and V as well as Fig. 5. The results are discussed in Secs. IV C and IV D.

C. Bound-state results

To evaluate the DOM's ability to describe the neutron bound-state region of the deformed nuclei ^{28}Si and ^{32}S, we compare predictions of E_{nlj}, N_{nlj}, R_{nlj}^{rms}, and S_{nlj} to available data. As a means of confirming and strengthening

our conclusions, we translate our neutron DOMs into proton DOMs, to take advantage of the substantial proton data that is available.

Results of our neutron DOM bound-state calculations for E_{nlj} and N_{nlj} are listed in Table IV, alongside experimental data. Our ^{28}Si DOM predicts $E_{nlj} = -51.9$ MeV for the $1s_{1/2}$ hole state, in agreement with the experimental value of -52 ± 15 MeV. We tuned our DOMs slightly to ensure that the $1s_{1/2}$ prediction for ^{32}S was somewhat deeper, at -53.2 MeV. Because the other neutron states in ^{28}Si are not resolved experimentally in Ref. [52], Table IV displays the energies for the combined $1p_{3/2}$ and $1p_{1/2}$ states and for the combined $1d_{5/2}$ and $2s_{1/2}$ states. The agreement between these experimental data and the DOM predictions is only fair. The DOM prediction for the energy separation between the $1s_{1/2}$ and $1p$ levels, of 21.4 MeV, easily agrees with the experimental value of 20 ± 16 MeV. However, the DOM prediction for the combined $1d_{5/2}$ and $2s_{1/2}$ levels, of 13.2 MeV, is too shallow compared to the experimental result of 17 ± 3 MeV.

The DOM predictions of N_{nlj} agree reasonably with the experimental data of Refs. [53,54], which have large uncertainties (about 30%). The predictions also agree well with the USD shell model calculations for the $1d_{5/2}$, $2s_{1/2}$, and $1d_{3/2}$ bound states. Experimental information for the $1f_{7/2}$ orbitals is scanty and, in addition, the measured N_{nlj} values are plagued with large uncertainties owing to weak excitation and strong fragmentation in one-nucleon transfer reactions [53]. Note that the DOM predictions of N_{nlj} for the $1f_{7/2}$ are half of those for the $1d_{3/2}$ orbitals.

Our predictions of N_{nlj} do not compare as well to the *mp-mh* CM calculations for the *s-d* orbitals, because the *mp-mh* CM
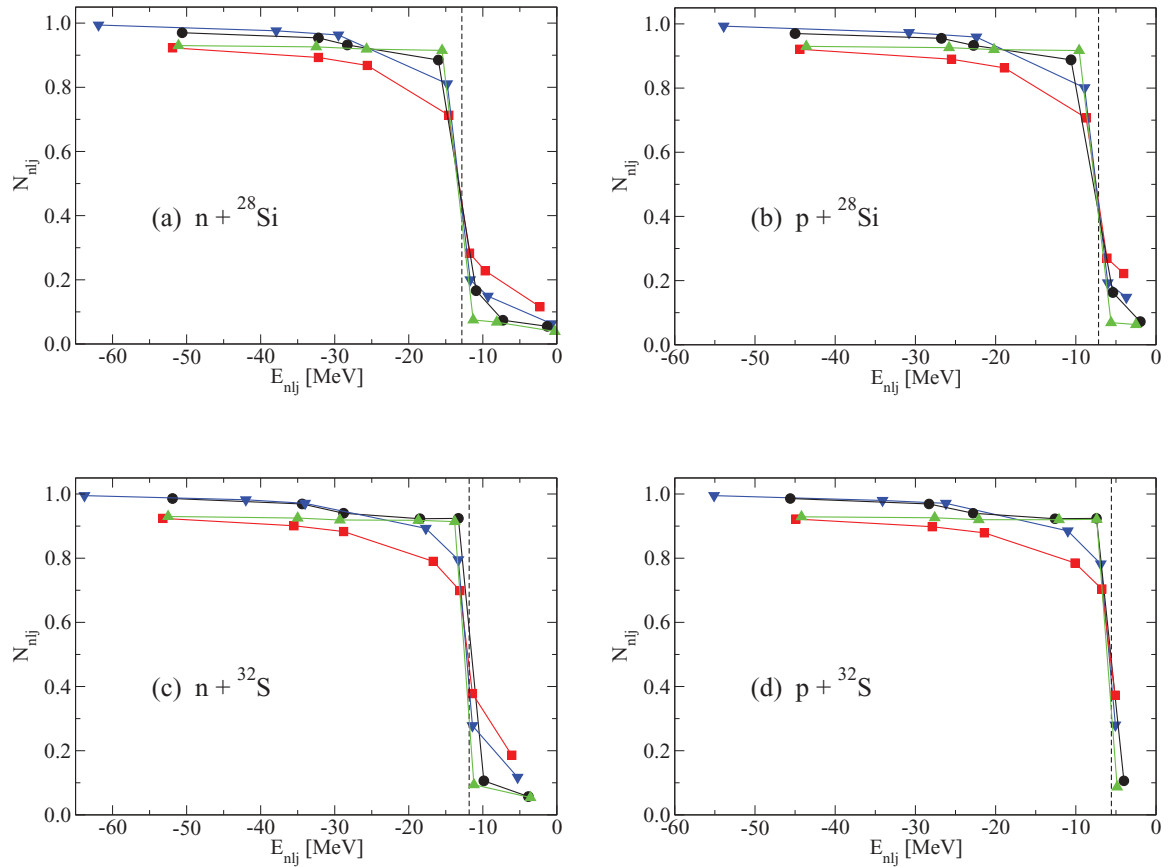
FIG. 5. (Color online) Calculations of occupation probability for (a) neutron orbitals in ^{28}Si, (b) proton orbitals in ^{28}Si, (c) neutron orbitals in ^{32}S, and (d) proton orbitals in ^{32}S. In each panel, we compare the predictions of the $V_{HF} + \Delta V_D$ DOM (blue downward triangles), the $V_{HF} + \Delta V_V$ DOM (green upward triangles), the full DOM (red squares), and the *mp-mh* CM calculations (black circles). The *mp-mh* CM results are plotted at single-particle energies that are obtained using mean-field calculations performed with the Gogny D1S effective force (see text for details).

calculations do not smear out as much around E_F. One reason for this is that the secular equation [Eq. (22)] conveys only part of the LRCs. A full account for LRCs would result from solving Eqs. (22) and (23) self-consistently. As a result of particle-vibration coupling, *dressed* single-particle orbitals would be defined and the orbital depletion would increase in the vicinity of E_F. However, the LRC depletion of about 2% presently calculated for the $1s_{1/2}$ deep-hole states is not expected to change significantly when the full LRCs are treated. Indeed, the finite-range character of the Gogny D1S effective force brings a natural cut to the high-energy particle-hole excitations [17].

Our DOM predictions of R_{nlj}^{rms} and S_{nlj} for the first particle and hole states are listed in Table VI (for both neutrons and protons). In evaluating these predictions, one must take special care in selecting experimental data. This is especially true for S_{nlj} data, which often are affected by normalization and measurement ambiguities that render them incomparable to DOM predictions (because the DOM predictions are computed relative to the independent particle value). To test our neutron predictions, we chose the recent consistent analysis of (p,d) and (d,p) transfer reactions of Ref. [55].

Our DOM predictions of R_{nlj}^{rms} for neutron orbitals in ^{28}Si and ^{32}S range from about 2.3 fm for $1s_{1/2}$ to about 4.2 fm for $1f_{7/2}$. For the $2s_{1/2}$ neutron particle state in ^{28}Si, our prediction

of 3.83 fm compares well to the experimental value of 3.73 ± 0.10 fm. For the $1d_{3/2}$ neutron particle state in ^{32}S, our prediction of 3.74 fm also compares well to the experimental value of 3.63 ± 0.10 fm. (We assigned uncertainties to the R_{nlj}^{rms} data of Ref. [55].)

Our prediction of S_{nlj} for the $2s_{1/2}$ neutron particle state in ^{28}Si is 0.603, which is higher than the experimental value of 0.42 ± 0.13 and the USD shell-model prediction of 0.45. For the $1d_{3/2}$ neutron particle state in ^{32}S, our prediction is 0.550, which is within uncertainties of the experimental result, of 0.70 ± 0.20, and compares reasonably to the USD prediction, of 0.61.

TABLE VI. Neutron and proton DOM predictions of rms radii, R_{nlj}^{rms} (fm), and spectroscopic factors, S_{nlj}, for the first particle and hole states.

	State	R_{nlj}^{rms} (fm)		S_{nlj}	
		Neutron	Proton	Neutron	Proton
^{28}Si	$2s_{1/2}$	3.83	4.01	0.603	0.619
	$1d_{5/2}$	3.43	3.52	0.572	0.571
^{32}S	$1d_{3/2}$	3.74	3.90	0.550	0.554
	$2s_{1/2}$	3.81	4.01	0.581	0.590

We next transformed our neutron DOMs into proton DOMs, to estimate the proton single-particle bound-state properties. We used the prescription of Ref. [15] for self-conjugate nuclei, in which the Coulomb correction is approximated as the difference between the proton and neutron Fermi energies, E_F. For the proton DOMs, all of the strength and geometry parameters in Table III were employed. Only two elements of the models were changed. First, we adopted new E_F values, which were recomputed using proton separation energies, yielding $E_F = -7.17$ MeV for ^{28}Si and -5.57 MeV for ^{32}S. Second, the Coulomb radii specified by Ref. [38] were used, the reduced values being 1.32 fm for ^{28}Si and 1.31 fm for ^{32}S. We checked our $p + ^{28}$Si DOM against the predictions of the "best" $p + ^{28}$Si OM of Ref. [38] and found reasonable agreement up to 60 MeV for $\sigma(\theta)$, $A_y(\theta)$, and the reaction cross section.

Results of our proton DOM calculations for E_{nlj} and N_{nlj} are displayed in Table V. Note that we organized the E_{nlj} data, culled from Refs. [56–60], into two columns labeled Exp. A and Exp. B. Comparison of our DOM predictions of E_{nlj} to experimental data shows mixed results. For ^{28}Si, the DOM prediction for the $1s_{1/2}$ state, of -44.4 MeV, overlaps with the measured value of -47.0 ± 4.0 MeV, but is too shallow compared to the other datum of -51 MeV. The DOM prediction of the energy separation between the $1s_{1/2}$ and $1p$ levels, 21.1 MeV, agrees reasonably with both sets of experimental data and also with the data displayed in Fig. 11 of Ref. [61]. The prediction for $1d_{5/2}$ is too shallow compared to data, while the predictions of $2s_{1/2}$ and $1d_{3/2}$ are too deep. For ^{32}S, the DOM predictions of E_{nlj} show a greater tendency to be shallow, although the result for the $2s_{1/2}$ orbital, -6.76 MeV, overlaps with the experimental value of -9 ± 3 MeV.

In comparing the N_{nlj} predictions in Tables IV and V, note that, because Coulomb effects play a minor role in the DOM and the *mp-mh* CM calculations, the predictions change only slightly for these models. The USD predictions are identical. As in the neutron case, the proton DOM results agree reasonably with the experimental data and with the USD predictions. Also, the *mp-mh* CM calculations yield N_{nlj} values near E_F that are too low for the particle states and too high for the holes.

We again made a careful review of the available experimental data for R_{nlj}^{rms} and S_{nlj} and chose the ^{32}S$(e,e'p)^{31}$P measurement of Ref. [62]. Overall, the proton DOM predictions for R_{nlj}^{rms} are slightly higher than the neutron predictions. However, for the $2s_{1/2}$ proton-hole state in ^{32}S, our DOM prediction of 4.01 fm is much higher than the experimental result of 3.59 ± 0.10 fm from Ref. [62]. This discrepancy raises the possibility that the proton DOMs should have different geometries than those for the neutron DOMs. We confirmed that the DOM predictions are sensitive to the geometrical parameters, but found that a complete account of the discrepancy would require a full proton DOM analysis (starting with fits to a proton-continuum database), which is out of the scope of the present work.

Our DOM predictions of S_{nlj} for the proton-hole valence orbitals, $1d_{5/2}$ in ^{28}Si and $2s_{1/2}$ in ^{32}S, are 0.571 and 0.590, respectively. The prediction for $2s_{1/2}$ in ^{32}S is lower than both the experimental value of 0.79 ± 0.07 from Ref. [62], and the USD prediction of 0.77. Our DOM predictions of S_{nlj} for the valence orbitals are slightly below the 60%–70% quenching of the independent-particle model value found from quasielastic electron scattering [63] and joint analyses of $(e, e'p)$ and $(d, ^3$He$)$ measurements for stable nuclei over the periodic table [64].

D. Long-range versus short-range correlations

Because LRCs and SRCs are cast in the OM potential components, both of these impact DOM predictions in the bound-state region. To help disentangle the interplay between LRC and SRC effects on N_{nlj}, we conducted two tests. Charity and co-workers [4] note that the surface-imaginary potential is associated with LRCs, while the volume-imaginary potential is associated with SRCs. Therefore, in the first test, we created variations of our DOMs in which one or the other of the dispersive corrections was turned off. The resulting predictions of N_{nlj} are shown in Fig. 5, for both ^{28}Si and ^{32}S (and for both neutron and proton orbitals). The colored symbols depend on whether the N_{nlj} are calculated using only $V_{\mathrm{HF}} + \Delta V_D$ (blue downward triangles), only $V_{\mathrm{HF}} + \Delta V_V$ (green upward triangles), or the full real potential $V_{\mathrm{HF}} + \Delta V_V + \Delta V_D$ (red squares). The predictions of the full DOMs are also listed in Tables IV and V.

Each set of symbols (connected by lines to guide the eye) displays similar patterns on the four panels of Fig. 5, reflecting the weak impact of the Coulomb field on predictions for both self-conjugate nuclei. The LRC-variant DOM (blue downward triangles) shows weak depletion for the deep hole states, of about 1%. For the higher states, the LRC depletion grows, reaching approximately 20% for the valence orbitals. In contrast, the SRC-variant DOM (green upward triangles) gives a depletion for the deep-hole states of about 10%. This compares well with the 13% SRC-dominant depletion amount found for the $1s_{1/2}$ and $1p_{3/2}$ proton orbitals in another light nucleus, ^{12}C, from $(e, e'p)$ measurements at high missing energies and momenta [65]. SRC depletion is approximately uniform over all of the hole states, in good agreement with microscopic model predictions [6,66]. For the valence orbitals, a combination of LRC and SRC effects in the full DOM (red squares) produces an overall orbital depletion (and quenching of spectroscopic factors) of about 30%, in good agreement with experimental results from quasielastic electron scattering [63] and from Green's function calculations [7].

Our second test used the *mp-mh* CM calculations to estimate the impact of LRC on N_{nlj}. These results are listed in Tables IV and V in the column labeled "CM" and appear as black circles in Fig. 5. The depletion is low for the deepest hole state, $1s_{1/2}$, and then increases for the valence orbitals. For the $1s_{1/2}$ orbitals, the *mp-mh* CM calculations give a depletion of about 2%. These bear a similarity to the DOM LRC variants (the downward blue triangles), which give a depletion of about 1%.

V. SUMMARY AND CONCLUSIONS

New neutron scattering measurements performed at TUNL between 8 and 18.9 MeV, as well as previous scattering and

reaction data available for ^{28}Si and ^{32}S, have been analyzed in the present study using the DOM, which was established about 25 years ago by Mahaux and Sartor for closed-shell nuclei. In applying the DOM to our open *sd*-shell nuclei, we fit the neutron DOMs to a large scattering database and extrapolated them to the bound-state regime. We then compared our DOM predictions of E_{nlj}, N_{nlj}, R_{nlj}^{rms}, and S_{nlj}, to the best available experimental data and to predictions of the USD shell model. We also extended the neutron DOMs to make predictions for proton bound-state quantities, taking advantage of a DOM prescription that is straightforward to implement for self-conjugate nuclei.

The overall agreement between the DOM predictions and measurements is only fair. In the scattering continuum, the neutron DOMs faced difficulties in fitting σ_T in the low-energy regime up to 25 MeV. Below about 15 MeV, the models also had some difficulty with the differential observables, especially at forward angles. In the bound-state region, our results are also mixed. The E_{nlj} predictions are reasonable for the deep-hole states but, otherwise, tend to be too shallow. The N_{nlj} predictions compare reasonably to the experimental data and to the USD predictions. The R_{nlj}^{rms} predictions compare well to the neutron data but are too large compared to the proton data. The neutron S_{nlj} predictions compare reasonably to the data but the proton predictions are low, close to the lower bound of the 60%–70% quenching of the independent-particle model value.

Both LRCs and SRCs affect the DOM predictions. We estimated the magnitude of LRC effects on N_{nlj} by performing *mp-mh* CM calculations for neutron and proton orbitals and also by generating variations of our DOMs in which one or the other of the dispersive corrections was turned off. The *mp-mh* CM calculations and the LRC variants of the DOM predict weak depletion for the deep-hole orbitals, while the full DOM predicts a depletion of the valence orbitals of about 30%. We conclude that SRCs dominate the depletion of the deep-hole orbitals, and gradually melt into LRCs when approaching the valence orbitals.

The merely adequate performance of our DOM parametrizations leads us to suggest a number of ways that they might be improved. One might be to consider phenomenological components other than central and spin-orbit potentials. Consideration of *l*- and parity-dependent components likely would improve the DOM fits to both the scattering and bound-state regions [49]. However, such an approach is not very appealing because it would add phenomenological parameters.

One limitation of our DOM parametrization is the assumption that the imaginary volume potential is symmetric with respect to E_F. This assumption is unreliable at large negative energies, as has been demonstrated previously in

a semiclassical OM approach [67] and more recently in the Green's function-based OM of Ref. [68]. Another limitation of our parametrization is the assumption that the DOM is local. Implementing a Gaussian-type of nonlocality in the imaginary potential (treated as on-shell) would remove the spurious energy dependence tied with the nonlocality cast in the dispersive potentials to a large extent [69]. Exploratory calculations along these lines show that DOM components calculated with and without nonlocality display MeV differences in their strengths [70]. More significant improvements are expected by using the nonlocality of the Perey-Buck type for the HF potential component, as has been discussed recently [71]. Full microscopic nonlocal DOM calculations in the bound-state region would shed light on the interpretation of spectral distributions deduced from $(e, e'p)$ measurements [62]. Although such calculations are highly desirable, their implementation for open-shell, deformed nuclei probably lie some years in the future. Implementing the microscopic DOM formalism with Gorkov-Green's functions [72] would be a step forward.

Finally, we hope that new, high-resolution (p, pn) and $(p, 2p)$ measurements will be performed, similar to those recently accomplished for ^{40}Ca in Ref. [73]. The determination of more reliable nucleon centroid energies for ^{28}Si and ^{32}S would allow us to better assess the reliability of the DOM. Of course, our calculations rely upon a spherical OM picture that ignores residual interactions originating from deformations. The DOM could be extended by including coupling to collective levels. This would require solving coupled-channel equations, not only for the continuum but also for the bound-state region. Because there is current interest in spherical OM potentials for the study of reactions in which one nucleon is added to or removed from a nucleus, an alternative strategy would be to evaluate the dynamic polarization potential originating from channel coupling, which is nonlocal, complex, and energy dependent [74]. The generalized DOM would then require the solution of Schrödinger equations implemented with nonlocal complex potentials. Pioneering efforts along these lines are presented in Refs. [75].

[1] F. Wrobel, Comput. Phys. Commun. **178**, 88 (2008), and references therein; M. B. Chadwick, Int. J. Rad. Bio. **88**, 10 (2012), and references therein.

[2] C. Mahaux and R. Sartor, Adv. Nucl. Phys. **20**, 1 (1991).

[3] R. J. Charity, L. G. Sobotka, and W. H. Dickhoff, Phys. Rev. Lett. **97**, 162503 (2006).

[4] R. J. Charity, J. M. Mueller, L. G. Sobotka, and W. H. Dickhoff, Phys. Rev. C **76**, 044314 (2007).

[5] J. M. Mueller *et al.*, Phys. Rev. C **83**, 064605 (2011).

[6] W. H. Dickhoff and C. Barbieri, Prog. Part. Nucl. Phys. **52**, 377 (2004).

[7] C. Barbieri, Phys. Rev. Lett. **103**, 202502 (2009).

[8] R. Subedi *et al.*, Science **320**, 1476 (2008); D. Higinbotham, E. Piasetzky, L. Weinstein, and S. A. Wood, J. Phys.: Conf. Ser. **299**, 012010 (2011); J. Arrington, D. W. Higinbotham, G. Rosner, and M. Sargsian, Prog. Part. Nucl. Phys. **67**, 898 (2012).

[9] J. P. Delaroche, M. S. Islam, and R. W. Finlay, Phys. Rev. C **33**, 1826 (1986).

[10] J. P. Delaroche, Y. Wang, and J. Rapaport, Phys. Rev. C **39**, 391 (1989).

[11] B. H. Wildenthal, Prog. Part. Nucl. Phys. **11**, 5 (1984); B. A. Brown and B. H. Wildenthal, Annu. Rev. Nucl. Part. Sci. **38**, 29 (1988).

[12] E. Caurier and F. Nowacki, Acta Phys. Pol. B **30**, 705 (1999).

[13] J. Vernotte, G. Berrier-Ronsin, J. Kalifa, R. Tamisier, and B. H. Wildenthal, Nucl. Phys. A **571**, 1 (1994).

[14] J. Vernotte, G. Berrier-Ronsin, S. Fortier, E. Hourani, A. Khendriche, J. M. Maison, J.-H. Rosier, G. Rotbard, E. Caurier, and F. Nowacki, Nucl. Phys. A **655**, 415 (1999).

[15] C. Mahaux and R. Sartor, Nucl. Phys. A **484**, 205 (1988); J.-P. Jeukenne, C. Mahaux, and R. Sartor, Phys. Rev. C **43**, 2211 (1991).

[16] N. Pillet, J. F. Berger, and E. Caurier, Phys. Rev. C **78**, 024305 (2008).

[17] N. Pillet, V. G. Zelevinsky, M. Dupuis, J.-F. Berger, and J. M. Daugas, Phys. Rev. C **85**, 044315 (2012).

[18] J. F. Berger, M. Girod, and D. Gogny, Comput. Phys. Commun. **63**, 385 (1991); J. Decharge and D. Gogny, Phys. Rev. C **21**, 1568 (1980).

[19] S. M. El-Kadi, C. E. Nelson, F. O. Purser, R. L. Walter, A. Beyerle, C. R. Gould, and L. W. Seagondollar, Nucl. Phys. A **390**, 509 (1982).

[20] H. H. Hogue, TUNL computer code EFFIGY (unpublished).

[21] W. Tornow, C. R. Howell, H. G. Pfutzner, M. L. Roberts, P. D. Felsher, Z. M. Chen, and R. L. Walter, Phys. Rev. C **35**, 1578 (1987).

[22] E. Woye and W. Tornow, TUNL computer code JANE (unpublished).

[23] S. Cierjacks, P. Forti, D. Kopsch, L. Kropp, J. Febe, and H. Unseld, Kernforschungszentrum Karlsruhe, Report KFK-1000, 1968.

[24] R. W. Finlay, W. P. Abfalterer, G. Fink, E. Montei, T. Adami, P. W. Lisowski, G. L. Morgan, and R. C. Haight, Phys. Rev. C **47**, 237 (1993).

[25] G. A. Petitt, S. G. Buccino, C. E. Hollandsworth, and P. R. Bevington, Nucl. Phys. A **79**, 231 (1966).

[26] W. E. Kinney and F. G. Perey, Report ORNL-4517, 1970.

[27] C. R. Howell, R. S. Pedroni, G. M. Honore, K. Murphy, R. C. Byrd, G. Tungate, and R. L. Walter, Phys. Rev. C **38**, 1552 (1988).

[28] J. Rapaport, J. D. Carlson, D. Bainum, T. S. Cheema, and R. W. Finlay, Nucl. Phys. A **286**, 232 (1977).

[29] A. Virdis, CEA Report No. CEA-R-5144, 1981.

[30] R. P. DeVito, Sam M. Austin, U. E. P. Berg, R. De Leo, and W. A. Sterrenburg, Phys. Rev. C **28**, 2530 (1983).

[31] E. L. Hjort, F. P. Brady, J. L. Romero, J. R. Drummond, D. S. Sorenson, J. H. Osborne, B. McEachern, and L. F. Hansen, Phys. Rev. C **50**, 275 (1994).

[32] W. P. Abfalterer, F. B. Bateman, F. S. Dietrich, R. W. Finlay, R. C. Haight, and G. L. Morgan, Phys. Rev. C **63**, 044608 (2001).

[33] B. Holmqvist, T. Wiedling, and M. Salama, Studsvik Energiteknik AB, Report AE-366, 6906, 1969.

[34] F. G. Perey and W. E. Kinney, Oak Ridge National Laboratory, Report ORNL-4539, 1970.

[35] J. C. Ferrer, J. D. Carlson, and J. Rapaport, Nucl. Phys. A **275**, 325 (1977).

[36] Y. Yamanouti, Nucl. Phys. A **283**, 23 (1977).

[37] J. S. Winfield, Sam M. Austin, R. P. DeVito, U. E. P. Berg, Ziping Chen, and W. Sterrenburg, Phys. Rev. C **33**, 1 (1986).

[38] A. J. Koning and J. P. Delaroche, Nucl. Phys. A **713**, 231 (2003).

[39] A. Ohrn *et al.*, Phys. Rev. C **77**, 024605 (2008).

[40] G. Haouat, Ch. Lagrange, R. de Swiniarski, F. S. Dietrich, J. P. Delaroche, and Y. Patin, Phys. Rev. C **30**, 1795 (1984).

[41] J. Raynal, Notes on ECIS94, CEA Saclay Report No. CEA-N-2772, 1994.

[42] Zuying Zhou *et al.*, Phys. Rev. C **82**, 024601 (2010).

[43] J. P. Delaroche and W. Tornow, Phys. Lett. B **203**, 4 (1988); G. J. Weisel *et al.*, Phys. Rev. C **54**, 2410 (1996); M. M. Nagadi *et al.*, *ibid.* **68**, 044610 (2003).

[44] C. H. Johnson and C. Mahaux, Phys. Rev. C **38**, 2589 (1988).

[45] C. Mahaux and R. Sartor, Nucl. Phys. A **493**, 157 (1989).

[46] A. J. Koning, S. Hilaire, and M. C. Duijvestijn, AIP Conf. Proc. **769**, 1154 (2005).

[47] P. Moldauer, Phys. Rev. C **14**, 764 (1976); Nucl. Phys. A **344**, 185 (1980).

[48] S. F. Mughabghab, M. Divadeenam, and N. E. Holden, *Neutron Cross Sections* (Academic Press, New York, 1981), Vol. 1.

[49] C. H. Johnson and R. R. Winters, Phys. Rev. C **27**, 416 (1983); R. R. Winters, C. H. Johnson, and A. D. MacKellar, *ibid.* **31**, 384 (1985); G. H. Rawitscher and D. Lukaszek, *ibid.* **69**, 044608 (2004).

[50] A. D. MacKellar and B. Castel, Phys. Rev. C **29**, 1993 (1984); **28**, 441 (1983).

[51] C. H. Johnson, Oak Ridge National Laboratory, 1990 (private communication).

[52] J. W. Watson, P. J. Pella, M. Ahmad, B. S. Flanders, N. S. Chant, P. G. Roos, D. W. Devins, and D. F. Friesel, J. Phys. Colloques **45**, C4-91 (1984).

[53] B. Castel, I. P. Johnstone, B. P. Singh, and J. C. Parikh, Nucl. Phys. A **157**, 137 (1970).

[54] F. Pellegrini, I. Filosofo, F. Gentilin, I. Scotoni, and I. Gabrielli, Nuovo Cimento A **65**, 297 (1970).

[55] Jenny Lee, M. B. Tsang, and W. G. Lynch, Phys. Rev. C **75**, 064320 (2007).

[56] J. Mougey, M. Bernheim, A. Bussiere, A. Gillebert, P. X. Ho, M. Priou, D. Royer, I. Sick, and G. J. Wagner, Nucl. Phys. A **262**, 461 (1976).

[57] G. Landand *et al.*, Nucl. Phys. A **173**, 337 (1971); S. Kullander *et al.*, *ibid.* **173**, 357 (1971).

[58] P. D. Cottle, Phys. Rev. C **76**, 027301 (2007).

[59] H. Tyren, S. Kullander, O. Sunderg, R. Ramachandran, P. Isaacson, and T. Berggren, Nucl. Phys. A **79**, 321 (1966).

[60] S. Frullani and J. Mougey, Adv. Nucl. Phys. **14**, 1 (1984).

[61] G. Jacob and Th. A. J. Maris, Rev. Mod. Phys. **45**, 6 (1973).

[62] J. Wesseling, C. W. de Jager, L. Lapikas, H. de Vries, M. N. Harakeh, N. Kalantar-Nayestanaki, L. W. Fagg, R. A. Lindgren, and D. Van Neck, Nucl. Phys. A **547**, 519 (1992).

[63] L. Lapikas, Nucl. Phys. A **553**, 297c (1993).

[64] G. J. Kramer, H. P. Blok, and L. Lapikas, Nucl. Phys. A **679**, 267 (2001).

[65] J. J. Kelly, Phys. Rev. C **71**, 064610 (2005), and references therein.

[66] A. Rios, W. H. Dickhoff, and A. Polls, J. Phys.: Conf. Ser. **312**, 022007 (2011); A. Rios, A. Polls, and W. H. Dickhoff, Phys. Rev. C **79**, 064308 (2009).

[67] R. W. Hasse and P. Schuck, Nucl. Phys. A **438**, 157 (1985).

[68] S. J. Waldecker, C. Barbieri, and W. H. Dickhoff, Phys. Rev. C **84**, 034616 (2011).

[69] C. Mahaux and R. Sartor, Nucl. Phys. A **458**, 25 (1986).

[70] P. Romain and J. P. Delaroche, in *Proceedings of a Specialists Meeting on Nucleon-Nucleus Optical Model up to 200 MeV, 13–15 November 1996, Bruyeres le Chatel, France* (OECD/NEA, 1997), p. 167, available at http://www.oecd-nea.org/science/om200.

[71] W. H. Dickhoff, D. Van Neck, S. J. Waldecker, R. J. Charity, and L. G. Sobotka, Phys. Rev. C **82**, 054306 (2010).

[72] V. Soma, T. Duguet, and C. Barbieri, Phys. Rev. C **84**, 064317 (2011).

[73] Y. Yasuda *et al.*, Phys. Rev. C **81**, 044315 (2010).

[74] N. K. Glendenning, *Direct Nuclear Reactions* (Academic Press, New York, 1983); P. Fraser, K. Amos, S. Karataglidis, L. Canton, G. Pisent, and J. P. Svenne, Eur. Phys. J. A **35**, 69 (2008).

[75] Raymond S. Mackintosh, Nucl. Phys. A **164**, 398 (1971); G. H. Rawitscher and G. Delic, Phys. Rev. C **29**, 1153 (1984); G. Cattapan, L. Canton, and G. Pisent, *ibid.* **43**, 1395 (1991).